Applied Catalysis B: Environmental 300 (2022) 120724

Contents lists available at ScienceDirect

Applied Catalysis B: Environmental

journal homepage: www.elsevier.com/locate/apcatb

Lorentz force promoted charge separation in a hierarchical, bandgap tuned, and charge reversible $Ni_xMn_{(0.5-x)}O$ photocatalyst for sulfamethoxazole degradation

Hassan Anwer [a], Jae-Woo Park [b,*]

[a] Department of Environmental Engineering, Izmir Institute of Technology, Urla, Izmir 35430, Turkey
[b] Department of Civil and Environmental Engineering, Hanyang University, 222 Wangsimni-ro, Seoul 04763, South Korea

ARTICLE INFO

Keywords:
Hierarchical catalyst
Lorentz force
Bandgap tuning
Magnetic separation
Sulfamethoxazole

ABSTRACT

Here, a hierarchical $Ni_xMn_{(0.5-x)}O$ catalyst that propels charge carriers to opposite interfaces of core@shell nanoparticle is reported. The opposite drift of charge carriers was achieved by tuning band edges in a multilevel catalyst by varying the molar concentration (x, 0→0.5) of precursors in a series of input injections. Preferential oxidation by holes on the surface of the catalyst was confirmed with the oxidation state transformation of metal ions (platinum and lead) deposited on the catalyst from their respective solutions. To obtain an electron rich surface, the synthesis scheme was reversed (x, 0.5→0), which yielded a catalyst with an inverse geometry and directed electron flow towards the surface. The collective impact of the Lorentz force and internal charge carrier drift contributed to excellent recombination suppression and 98% sulfamethoxazole degradation in 30 min. Finally, structural integrity and catalytic potential of the composite after repeated magnetic separation and degradation cycles was assessed to establish its practical applicability.

1. Introduction

Photocatalysis harnesses solar energy for chemical synthesis, water/air purification, and energy generation by water splitting [1]. The product yield of these photochemical processes depends strongly on the efficacy of exciton generation and the charge carrier lifetime [2]. Charge carrier performance in a reaction can be improved by: (i) material modification and (ii) using external agents to supplement the catalytic activity of composites. Material modification using surface and interface engineering approaches were proposed to increase electron–hole relaxation time. Semiconductor combinations formed between Type I and II heterostructures, such as solid state z–scheme [3,4], direct z–scheme [5], p–n [6], and n–n junctions [7] improved charge separation by an interfacial electric field due to band edge alignment. A Schottky junction, which is formed between a metal (Pt) and a semiconductor (ZnO), induced band bending due to the higher work function of the metal [8]. It confines electrons in the metal and holes on the semiconductor surface. Schottky junctions were also created using other conductive materials, such as carbon nanotubes [9], graphene [10,11], carbides [12], and nanosheets of transition metal dichalcogenides [13]. Synergistic utilization of plasmonic effect and Schottky junction increased visible light activity and charge carrier lifespan in a copper–mediated metal–organic framework, resulting in a highly oxidative conversion of benzylic alcohols [14]. Facet dependent charge separation using Bi metal deposited on BiOBr nanosheets increased the generation of reactive oxygen species (ROS) in the reaction mixture [15]. Continuous efforts have been made to find new and hybridized approaches to suppress recombination, but it remains a major obstacle that hinders more efficient applications of photocatalysis.

Effective separation of catalysts from reactant/product mixtures is required to prevent secondary contamination and reuse catalysts for practical applications. Deposition of catalysts on supporting substrates using (i) binder–through (organic [16] and inorganic [17]) and (ii) binder–less (spray coating [18], hot pressing [19], in–situ growth [20], and electrophoretic [21]) methods, results in the masking of active sites, reducing the surface areas of catalysts. Magnetically–separable nano–-sized catalysts, such as CeO_2, C_3N_4, graphene oxide, CdZnS, ZnO, $ZnFe_2O_4$, and TiO_2 can potentially facilitate the separation while retaining the intrinsic activity and specific surface area [22–26]. Composites of magnetic and catalyst materials, however, can suffer from haphazard interfacial contact between magnetic and catalyst parts, which is critical for nanomaterial separation efficiency. Core@shell

* Correspondence to: Department of Civil and Environmental Engineering, Hanyang University, Seoul, South Korea.
E-mail address: jaewoopark@hanyang.ac.kr (J.-W. Park).

https://doi.org/10.1016/j.apcatb.2021.120724
Received 11 July 2021; Received in revised form 7 September 2021; Accepted 11 September 2021
Available online 15 September 2021

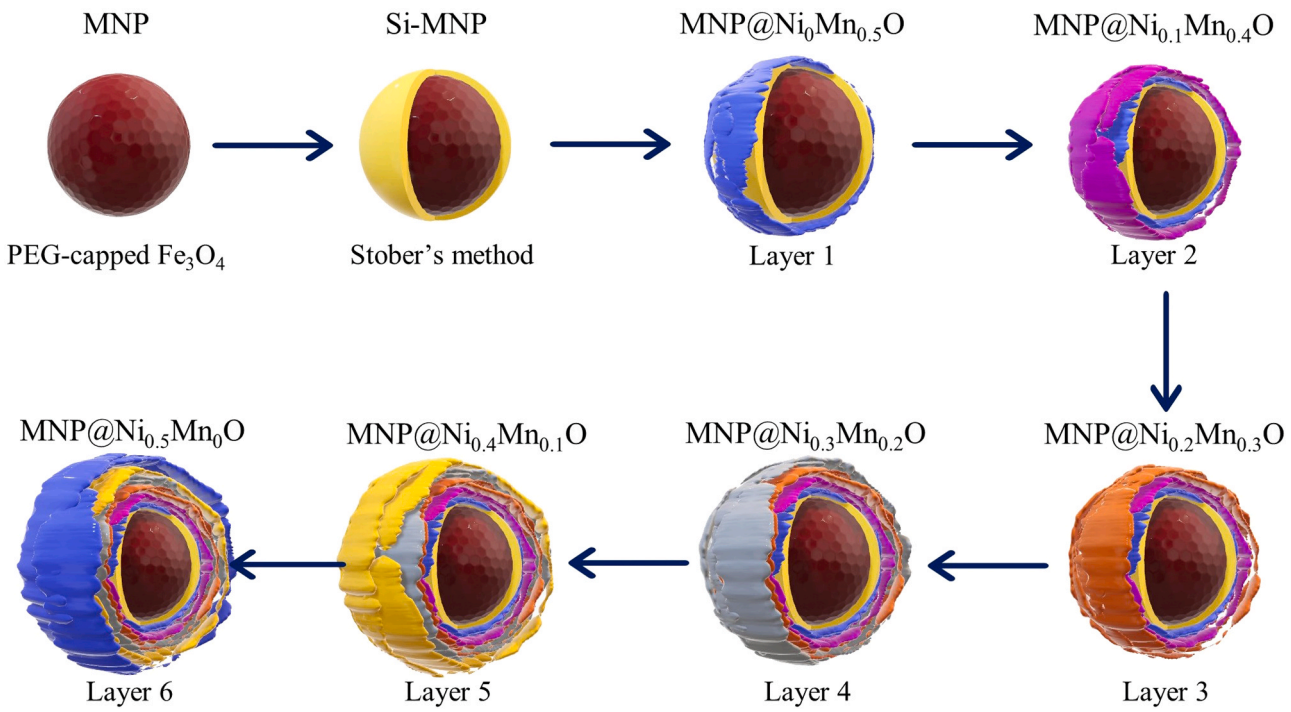

Fig. 1. Growth of hierarchical layers with stepwise precursor injections.

composites with relatively better morphology and magnetic separation were fabricated with perovskite oxides [27], Bi_2O_3 [28], NiO [29], WO_3 [30], and K_xMnO_2 [31]. Core@shell composites exhibited high charge recombination due to a simple catalyst formulation and the absence of heterostructure/Schottky junctions. Overall, a novel composite with excellent interfacial contact between (i) surface–engineered catalyst with a longer charge lifetime and (ii) magnetic core for separation is highly desired.

A new catalyst composite ($Ni_xMn_{(0.5-x)}O$) with the previously mentioned qualities is proposed in this research. Uniform multilayers of $Ni_xMn_{(0.5-x)}O$ with tuned band edges in each layer were synthesized over magnetic nanoparticles (MNPs). Tuned band edges and the corresponding energy gradient provide an internal electric field that inhibits charge carrier recombination. The fabrication scheme in this research is practically interesting since either hole or electron abundant nanoparticle surface can be formed. A hole dominant surface can be achieved in $Ni_xMn_{(0.5-x)}O$ catalyst, and the molar concentration of Ni– and Mn–precursors can be inverted to form $Mn_xNi_{(0.5-x)}O$ for electron dominance.

Charge separation in nanomaterials can be supplemented using external agents. Hole–consuming/electron–donating sacrificial reagents (methanol, ethanol, and isopropanol) were used to achieve a high H_2 evolution rate of 2839 μg h^{-1} [32]. Photocatalytic degradation of gaseous toluene was enhanced by 11% with ozone addition to a graphene oxide/ZnO catalyst [33]. Ultrasound waves added to a MgO@CNT heterojunction composite improved photocatalytic degradation of sulfadiazine by 30% [34]. The external voltage effect on band bending and electric fields in nanomaterials has been well studied [35]. Recently, magnetic field–enhanced charge separation for photocatalytic H_2 evolution [36], organics degradation [37], and O_2 reduction were reported [38]. Magnetic fields can be generated using permanent magnets. In contrast to other external enhancement approaches, magnetic fields are durable and do not require strenuous maintenance and operational expenses. Photogenerated electrons and holes in moving nanoparticles are propelled in opposite directions due to the Lorentz force generated by a magnetic field. In this study, the external Lorentz force and internal charge separation were combined to maximize the charge carrier lifetime in novel MNP@$Ni_xMn_{(0.5-x)}O$ catalyst. To the best of our knowledge, this is the first report that investigates the Lorentz force effect on magnetically–separable catalysts. Sulfamethoxazole (SMZ) is a widely used antibiotic, and it is toxic to microorganisms, aquatic animals, and algae [39]. It can induce drug resistance and the generation of resistant genes. Here, the combined effect of Lorentz force and MNP@$Ni_xMn_{(0.5-x)}O$ on charge separation is assessed in SMZ photodegradation.

2. Experimental

2.1. Materials

Ferric chloride hexahydrate ($FeCl_3.6H_2O$, ≥99%), polyethylene glycol (PEG 1000, $H(OCH_2CH_2)_nOH$), sodium acetate (CH_3COONa, ≥99%), ethylene glycol ($HOCH_2CH_2OH$, ≥99%), tetraethyl ortho silicate (TEOS, $Si(OC_2H_5)_4$, 98%), urea (NH_2CONH_2, 99%), manganese nitrate tetrahydrate ($Mn(NO_3)_2.4H_2O$, 98%), lead nitrate ($Pb(NO_3)_2$, ≥ 99%), and nickel nitrate hexahydrate ($Ni(NO_3)_2.6H_2O$, 99%) were purchased from Sigma Aldrich, USA. Ethylene diamine tetraacetic acid (EDTA, $C_{10}H_{16}N_2O_8$, 99.5%) and dimethyl sulfoxide (DMSO, C_2H_6OS, 99.8%) were purchased from Junsei, Japan.

2.2. MNPs

As in a typical solvothermal method, $FeCl_3.6H_2O$ (3.24 g), PEG (2.4 g), and sodium acetate (8.64 g) were dissolved in 96 mL of ethylene glycol (Fig. S1). The mixture was vigorously stirred for 30 min and sonicated for 10 min to ensure complete dissolution. The solution was transferred to a 120 mL Teflon vessel and heated at 200 °C for 8 h. The black precipitates were washed five times with deionized (DI) water and ethanol. Subsequently, they were oven dried at 60 °C to produce MNPs.

2.3. MNP functionalization

Silica shell was grown on the MNPs by the Stober method [40]. The MNPs (500 mg) were dispersed in an ethanol (150 mL) and DI water (50

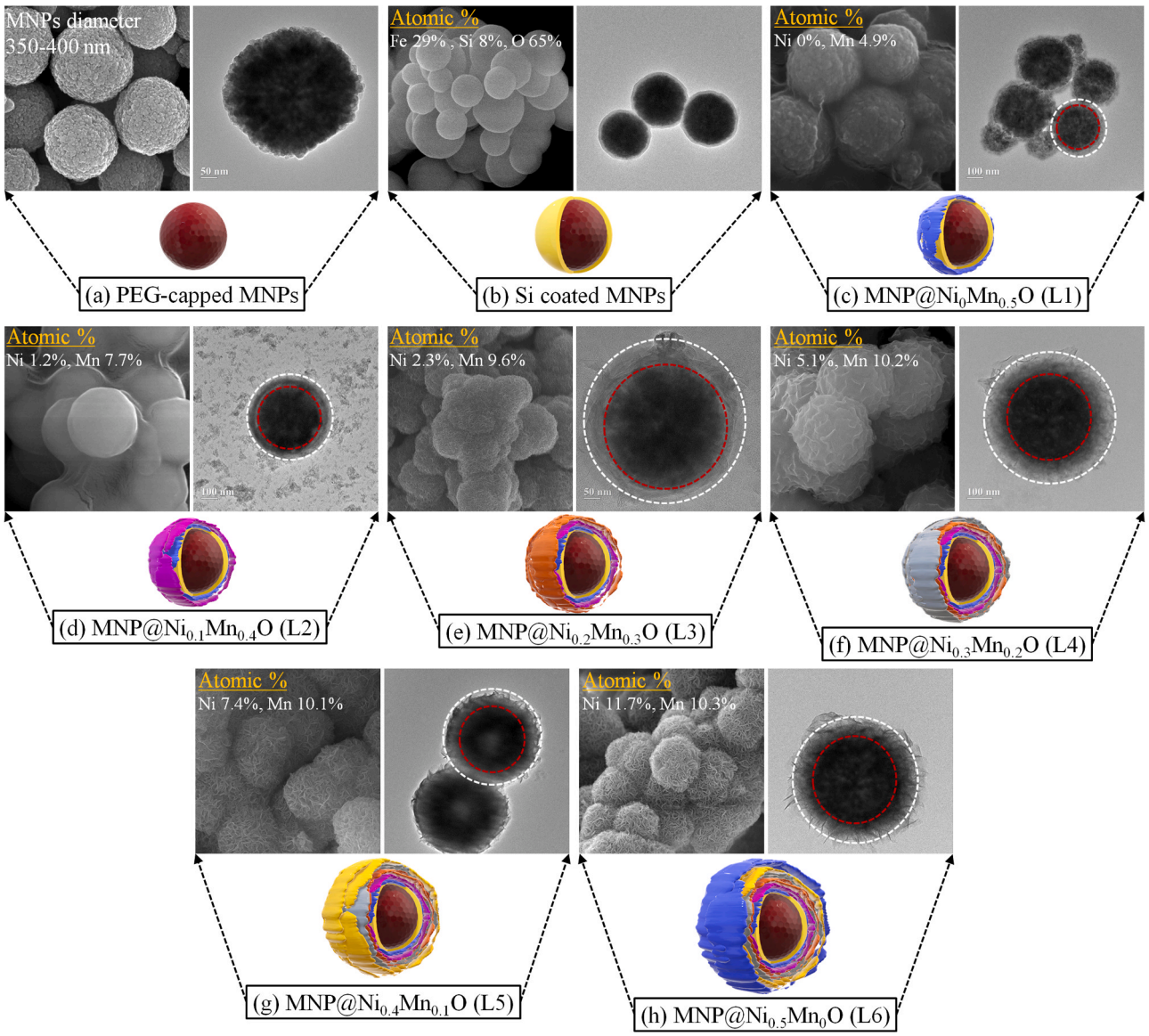

Fig. 2. SEM and TEM images of (a) PEG-capped MNPs, (b) Si coated MNPs, (c) MNP@$Ni_0Mn_{0.5}O$, (d) MNP@$Ni_{0.1}Mn_{0.4}O$, (e) MNP@$Ni_{0.2}Mn_{0.3}O$, (f) MNP@$Ni_{0.3}Mn_{0.2}O$, (g) MNP@$Ni_{0.4}Mn_{0.1}O$, and (h) MNP@$Ni_{0.5}Mn_0O$.

mL) mixture with 30 min sonication. Five milliliters of NH_4OH were added to the suspension, and it was sonicated for 5 min. TEOS (0.3 mL) was dissolved in ethanol (50 mL) and added dropwise to the MNP suspension under vigorous stirring in a rotary evaporator. The suspension was stirred at room temperature for 8 h. Silica–coated MNPs (Si–MNPs) were separated using a magnet and washed several times with DI water and ethanol. They were dried in an oven at 60 °C. The Si–MNPs were subjected to UV/plasma treatment to improve wettability, surface functionalities, and roughness for subsequent catalyst growth.

2.4. *MNP@$Ni_xMn_{(0.5-x)}O$ synthesis*

The hierarchical band gap catalyst in this research, MNP@$Ni_xMn_{(0.5-x)}O$, was synthesized in six steps (Fig. 1). The x in the subscript represents the millimoles of $Ni(NO_3)_2.6H_2O$. Initially, 150 mg of Si–MNPs were added in 200 mL DI water with 30 min ultrasonication. Urea (2.4 g) and 125 mg (0.5 mmol) of $Mn(NO_3)_2.4H_2O$ were dissolved in the MNP suspension and stirred in a rotary evaporator at 70 °C for 6 h (Fig. S1). The suspension was sonicated for 5 min, and 1 mL NH_4OH was added. It was kept in a rotary evaporator at 50 °C for 4 h to obtain $Ni_0Mn_{0.5}O$ (layer 1 (L1)). The solution was drained, and a fresh 200 mL solution containing urea (2.4 g), $Mn(NO_3)_2.4H_2O$ (100 mg, 0.4 mmol), and $Ni(NO_3)_2.6H_2O$ (29 mg, 0.1 mmol) was added. Then, the solution was stirred in a rotary evaporator at 70 °C for 6 h, sonicated for 5 min, and 1 mL of NH_4OH was added. It was kept in a rotary evaporator at 50 °C for 4 h to obtain L2 ($Ni_{0.1}Mn_{0.4}O$). In subsequent steps, L3 ($Ni_{0.2}Mn_{0.3}O$), L4($Ni_{0.3}Mn_{0.2}O$), L5($Ni_{0.4}Mn_{0.1}O$), and L6 ($Ni_{0.5}Mn_0O$) were synthesized in–situ by draining/replacing the precursor solution in each step. Finally, the MNP@$Ni_xMn_{(0.5-x)}O$ were washed, dried, and calcined in argon at 400 °C for 3 h. The MNP@$Ni_xMn_{(0.5-x)}O$ composite was washed thoroughly after calcination and dried at 60 °C overnight.

3. Results and discussion

3.1. *Characterization*

Morphological evolution of the MNP@$Ni_xMn_{(0.5-x)}O$ catalyst in each step is shown in Fig. 2. Original PEG–capped MNPs, which were spherical in shape with a rough surface texture, had diameters of 350–400 nm (Fig. 2(a)). A 25–30 nm thick silica shell was grown on the

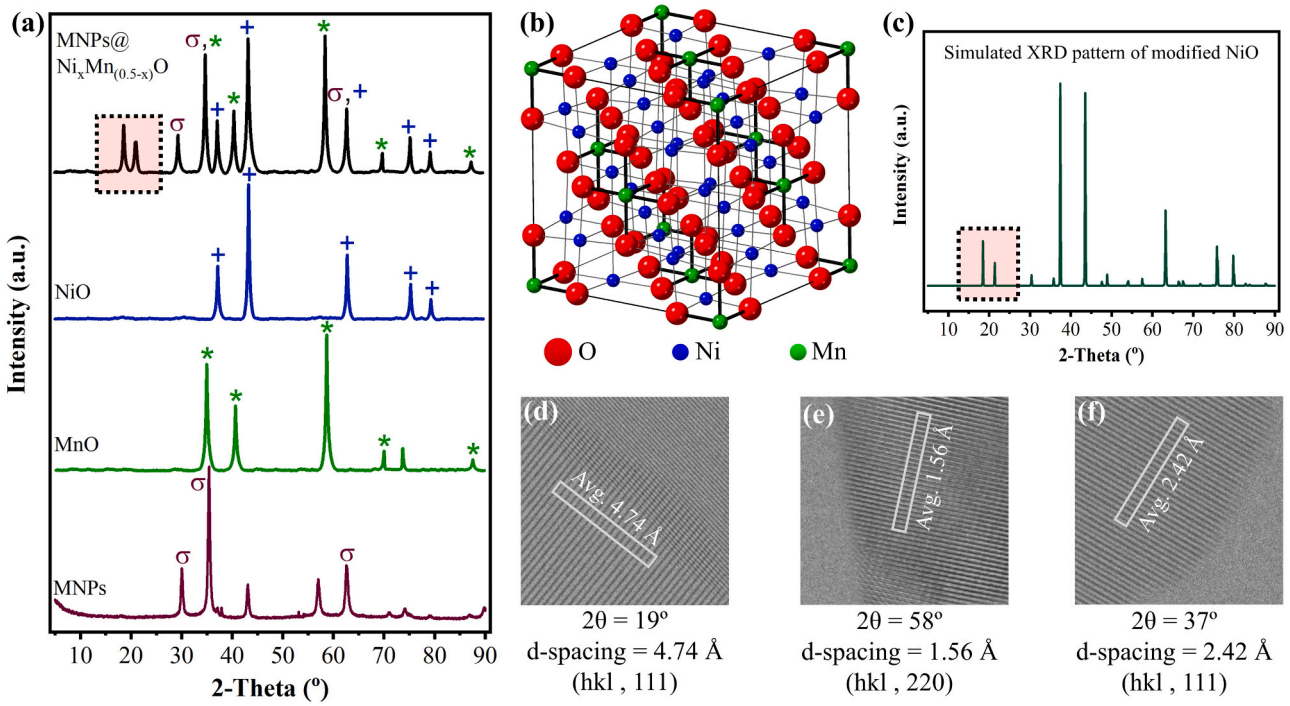

Fig. 3. (a) Experimental XRD spectra of MNPs, MnO, NiO, and MNP@$Ni_xMn_{(0.5-x)}O$. (b) Modified NiO unit cell having one eighth of Ni–atoms replaced by Mn–atoms. (c) Simulated XRD pattern of modified NiO unit cell. HRTEM images of (d) MNP@$Ni_xMn_{(0.5-x)}O$, (e) MnO, and (f) NiO.

PEG-capped MNPs to overcome the passivation due to PEG ligands (Fig. 2(b)). The Si–coated MNPs were treated with UV/plasma to obtain a super–hydrophilic surface before catalyst growth. UV/plasma treatment increased surface coarseness, which benefited metal–ion adsorption onto the nanoparticle surface [41]. The primary catalyst layer (L1) contained MnO that formed a smooth coating film in Fig. 2(c). Ni was supplemented from L2 ($Ni_{0.1}Mn_{0.4}O$) (Fig. 2(d)). The morphology of MNP@$Ni_xMn_{(0.5-x)}O$ evolved with increasing Ni content in the catalyst layer as shown in Fig. 2(e)–(h). The smooth film–like texture of Mn content in core layers (L1, L2, and L3) was covered with a flower–like structure with increasing Ni content in the outer layers (L4 and L5). Finally, highly porous surfaces covered with scales were obtained after injection of pure Ni–precursor in the outermost layer (L6) in Fig. 2(h). MNP@$Ni_xMn_{(0.5-x)}O$ catalyst was designed to sustain hole–based surface reactions under irradiation. An inverted analog of MNP@$Ni_xMn_{(0.5-x)}O$, MNP@$Mn_xNi_{(0.5-x)}O$, was synthesized to obtain an electron rich surface. MNP@$Mn_xNi_{(0.5-x)}O$ showed a smooth catalyst coating that differed from the flower–like surface of MNP@$Ni_xMn_{(0.5-x)}O$ (Fig. S2). Morphological analysis confirmed the robustness of the synthesis method used to obtain uniform core@shell nanoparticles. Moreover, the low concentration and stepwise synthesis approach showed promising results to invert the catalyst geometry, which is of great practical interest.

Structural and phase development of the magnetic photocatalyst was investigated using X–ray diffraction (XRD) and high–resolution transmission electron microscopy (HRTEM). XRD spectra of MNPs present two possible phases of magnetite and maghemite, which are difficult to differentiate due to their similar diffraction patterns. No diffraction peak was observed at 26°, which would correspond to the (211)–plane of maghemite. This confirmed the magnetite phase of the MNPs (Fig. 3(a)) [42]. The catalysts, MnO and NiO, were synthesized to understand their roles in the final composite of MNP@$Ni_xMn_{(0.5-x)}O$. In the MnO spectrum, a peak at 34° indicates a cubic structure (space group Fm3m, lattice parameters a=4.45 Å), which is a signature (111)–plane signal of the manganosite phase (JCPDS# 07-0230). The absence of diffraction peaks at 32° and 36°, corresponding to Mn_2O_3 (222) and Mn_2O_4 (211), respectively, confirmed the monoxide composition of Mn–catalyst. The XRD pattern of NiO suggests a face–centered cubic structure with two characteristic peaks at 37° and 43° resulting from the (111)– and (200)–planes, respectively, in the bunsenite phase of NiO (JCPDS# 78-0423). Peaks associated with the $Ni(OH)_2$ planes (001) and (011) were not detected at 19° and 38°, respectively, confirming the conversion of any residual hydroxides during calcination. The XRD spectrum of MNP@$Ni_xMn_{(0.5-x)}O$ consisted of diffraction peaks from pristine MNPs, MnO, and NiO, which are labeled accordingly in Fig. 3(a). Two additional peaks at 18° and 21°, missing in pristine MNPs, MnO, and NiO, were observed in MNP@$Ni_xMn_{(0.5-x)}O$. This suggested that a hybrid crystal structure was developed during the mixed precursor injections to obtain a multi–level catalyst assembly. To investigate the hybrid structure, one eighth of Ni–atoms were replaced by Mn–atoms in the NiO unit cell. Both were octahedrally coordinated by six oxygen atoms (Fig. 3(b)). The modified unit cell was used to render an XRD pattern. Two unidentified peaks in MNP@$Ni_xMn_{(0.5-x)}O$ appeared at the same 2θ positions in the simulated XRD pattern of NiO (Fig. 3(c)), confirming the presence of hybrid NiO–MnO along the pristine domains of NiO and MnO. HRTEM confirmed the hybrid crystal structure by revealing lattice fringes with a large d–spacing (4.74 Å) (Fig. 3(d)), which agreed with the reflection from a (111)–plane at 19° in MNP@$Ni_xMn_{(0.5-x)}O$ (Fig. 3 (a)). HRTEM of pristine MnO and NiO showed fringes of 1.56 Å (Fig. 3 (e)) and 2.42 Å (Fig. 3(f)), respectively. Fringes of d–spacings greater than 2.5 Å were not seen in the HRTEM of pristine NiO and MnO.

Elemental oxidation states in MNP@$Ni_xMn_{(0.5-x)}O$ hierarchical catalyst were investigated using X–ray photoelectron spectroscopy (XPS). In Fig. 4(a), Fe2p showed two core–level peaks at 709.5 and 711 eV, confirming the mixed oxide form of Fe^{2+} and Fe^{3+} in the magnetite phase (NIST CAS#1317619). The binding energy peak at 724.5 eV is a 2p1/2 spin–orbit component of the 2p3/2 peak at 711 eV, which is characteristic of Fe^{3+} compounds [43]. Fe^{3+} existed about two times more often than Fe^{2+} species in the XPS spectrum. Satellite peaks of Fe^{2+} and Fe^{3+} appeared at 715 and 720 eV, respectively. The Ni2p spectrum showed a mixture of core–level and satellite peaks (Fig. 4(b)). Binding energy signals at 854 and 871.4 eV are multiple split peaks

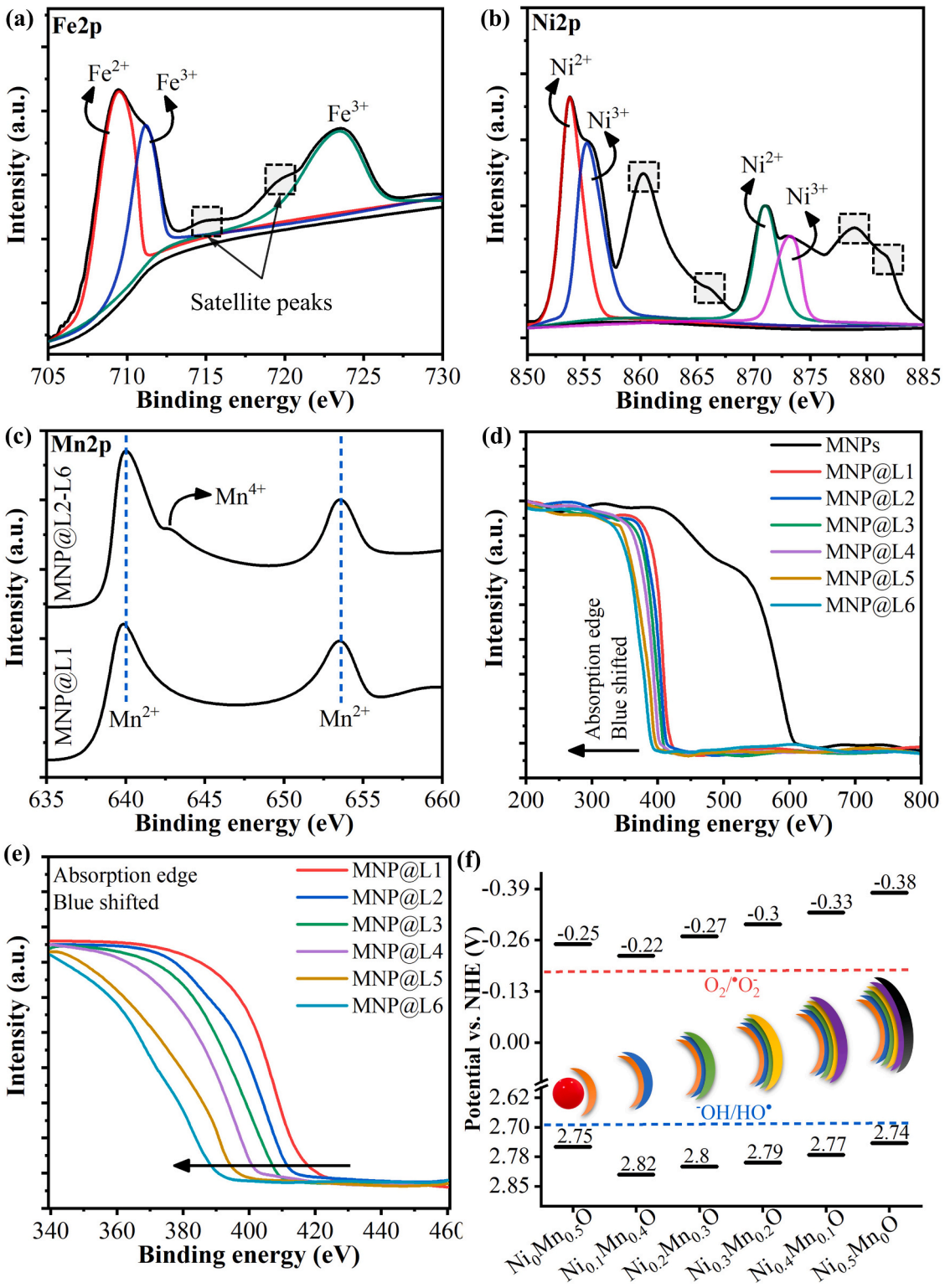

Fig. 4. XPS spectra of (a) Fe, (b) Ni, and (c) Mn. (d and e) UV–vis light absorption spectrum of the composites. (f) Change in conduction and valence band position of the composites with the growth of catalyst layers.

associated with Ni(II) oxide (NIST CAS#1313-99-1). Some Ni^{2+} cations were transformed to Ni^{3+} after calcination in argon, suggesting that Ni_2O_3 coexisted with NiO. Ni^{3+} were identified by the 855.4 and 873 eV peaks in the XPS spectrum (NIST CAS#1314063). Satellite peaks arising due to the main Ni2p peaks are indicated in the square boxes. The peaks at 640 and 653 eV in Fig. 4(c) confirmed the Mn(II) oxide form in the primary catalyst layer MNP@L1 (NIST CAS#1344-43-0). A shoulder peak at 642.5 eV, corresponding to Mn^{4+}, was observed after mixed precursor injections after MNP@L1. This binding energy of 642.5 eV is correlated with that of Mn^{4+} in MnO_2 (NIST CAS#1313-13-9), which can be caused by metal cations or Mn defects due to diffusion of Mn atoms in the NiO unit cell.

Light absorption by the catalysts was analyzed using UV–vis diffuse reflectance spectroscopy (DRS). Pristine MNPs exhibited light

Table 1
Band gap/edge of different layers in the hierarchical catalyst.

Composite	Layer#	Composition		Bandgap (eV)	Band edge vs. NHE (eV)	
		Mn	Ni		VB	CB
$Ni_0Mn_{0.5}O$	L1	0.5	0.0	3.00	2.75	–0.25
$Ni_{0.1}Mn_{0.4}O$	L2	0.4	0.1	3.04	2.82	–0.22
$Ni_{0.2}Mn_{0.3}O$	L3	0.3	0.2	3.07	2.80	–0.27
$Ni_{0.3}Mn_{0.2}O$	L4	0.2	0.3	3.09	2.79	–0.30
$Ni_{0.4}Mn_{0.1}O$	L5	0.1	0.4	3.10	2.77	–0.33
$Ni_{0.5}Mn_0O$	L6	0.0	0.5	3.12	2.74	–0.38

absorption in a wide spectral range that extended up to the red portion of visible light (Fig. 4(d)). Catalyst deposition limited light absorption of the MNPs by blocking the yellow and green fragments of the visible spectrum. A hypsochromic shift was observed with increasing Ni–content in the catalyst layers (Fig. 4(e)). DRS and Tauq plots showed that the band gap increased from 3.02 eV in L1 to 3.12 eV in L6. Band edge positions of the catalysts determined with ultraviolet photoelectron spectroscopy (UPS) are listed in Table 1. The conduction band minimum (CBM) was lifted with increasing Ni% in the outer catalyst layers. The oxygen vacancies associated with Ni–unit cells donated electrons to the metal cations, which added electronic states closer to CBM and increased both the fermi level and CBM [44]. Conversely, the valence band maximum (VBM) was shifted down to a higher oxidation potential in the inner catalyst layers (except L1). The diffusion of Mn–ions into NiO unit cells, as seen in XRD spectra, created cation vacancies that added new electronic levels near the VBM of L2, L3, L4, and L5 [45]. This conclusion was strengthened by the VBM position in L1, which arose due to the absence of cationic vacancies (Fig. 4(f)). Intrinsic electronic structure and vacancy defects generated a gradient in the band structure that could direct holes toward the nanoparticle surface (Fig. 4(f)). Charge carrier direction can be inverted by reversing the synthesis scheme to obtain an electron rich surface. UV–active catalysts with a large band gap were chosen to study $^{\bullet}OH$ and $^{\bullet}O_2^-$ radical generation before (Fig. S3(a)) and after (Fig. S3(b)) catalyst inversion, respectively. A visible light active catalyst can be fabricated using our synthesis approach. A smaller band gap catalyst can be tuned to regulate either $^{\bullet}O_2^-$ or $^{\bullet}OH$ dominant surface reactions in Fig. S3(c) and (e), respectively). Inverted counterparts of visible light active catalysts will not work due to limitations of bandgap tuning in Fig. S3(d) and (f), which will be discussed in an evaluation of the performance results.

3.2. Performance evaluation

Band edges in hierarchical MNP@$Ni_xMn_{(0.5-x)}O$ were engineered to drive holes toward the nanoparticle surface. The abundance of holes on the surface was investigated by suspending the nanocomposite in a metal precursor solution containing lead (Pb) ions (SI Note 1). The suspension was irradiated, and the change in the oxidation state of Pb–species deposited on MNP@$Ni_xMn_{(0.5-x)}O$ was monitored using XPS. In Fig. 5(a), the Pb4f spectrum indicates that Pb^{2+} in solution was

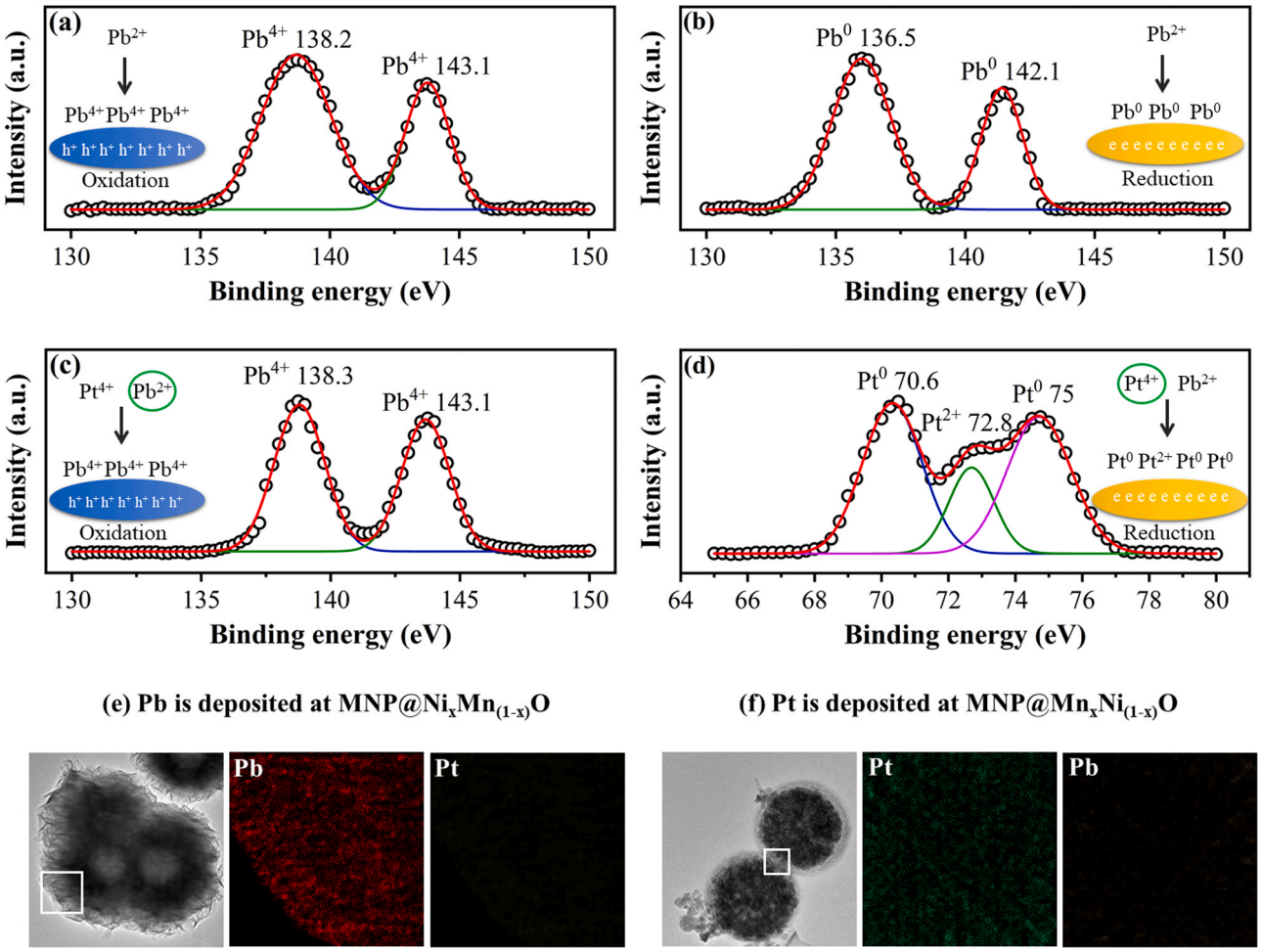

Fig. 5. XPS spectra showing Pb^{2+} transformation on (a) MNP@$Ni_xMn_{(0.5-x)}O$ and (b) MNP@$Mn_xNi_{(0.5-x)}O$. (c) XPS spectrum of MNP@$Ni_xMn_{(0.5-x)}O$ highlighting its selectivity for Pb^{2+} ions. (d) XPS spectrum of MNP@$Mn_xNi_{(0.5-x)}O$ highlighting its selectivity for $PtCl_6^{2-}$ ions. (e) and (f) TEM/HRTEM images of MNP@$Ni_xMn_{(0.5-x)}O$ and MNP@$Mn_xNi_{(0.5-x)}O$, respectively.

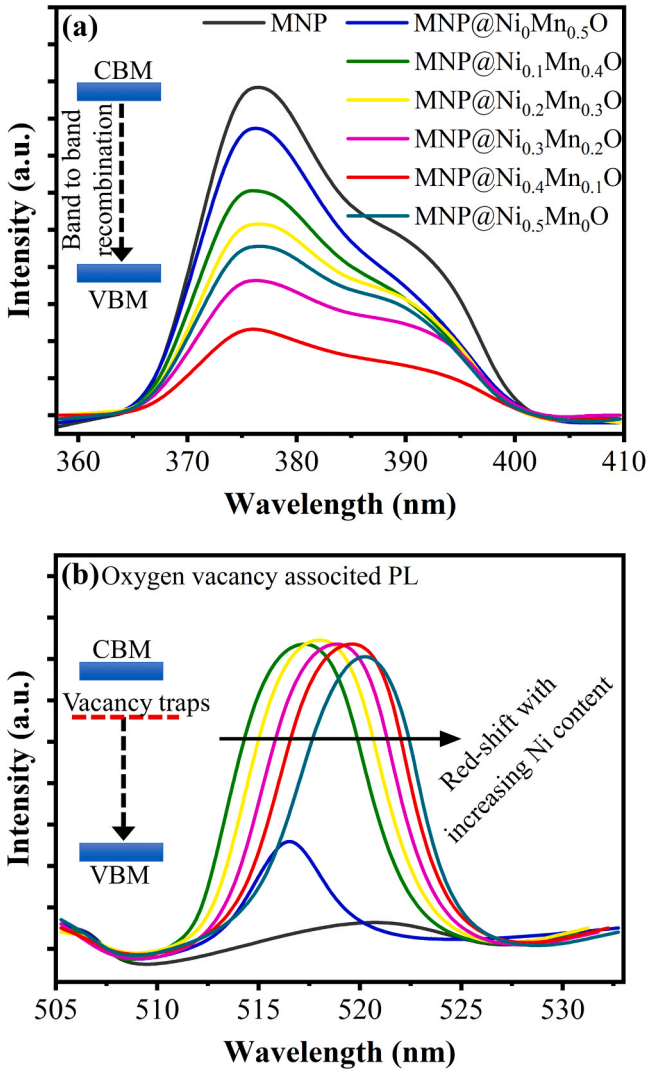

Fig. 6. Photoluminescence spectra of the composites originating from (a) band to band recombination and (b) indirect electron relaxation via oxygen vacancy traps.

transformed to Pb^{4+} (PbO_2), confirming the dominance of hole–driven oxidation reactions on MNP@$Ni_xMn_{(0.5–x)}O$. The inverted counterpart of MNP@$Ni_xMn_{(0.5–x)}O$, MNP@$Mn_xNi_{(0.5–x)}O$, was used in the Pb metal–ion deposition experiment. XPS results showed that Pb^{2+} was converted to Pb^0 (Fig. 5(b)), which indicated that we achieved charge reversibility by inverting the catalyst geometry. Photooxidation and photoreduction were achieved due to an energy gradient that guided the holes and electrons toward the particle surface in MNP@$Ni_xMn_{(0.5–x)}O$ and MNP@$Mn_xNi_{(0.5–x)}O$, respectively. These results imply that selective oxidation or reduction can be regulated in a photochemical reaction by choosing the catalyst accordingly. Charge carrier separation and selectivity of the nanocomposites were further investigated in a joint metal–ion deposition test. MNP@$Ni_xMn_{(0.5–x)}O$ and MNP@$Mn_xNi_{(0.5–x)}O$ were separately suspended in a precursor solution containing Pb^{2+} and $PtCl_6^{2-}$ ions. After irradiation, the nanocomposites were magnetically separated and analyzed using XPS. The MNP@$Ni_xMn_{(0.5–x)}O$ spectrum indicated the presence of Pb, while peaks associated with Pt were not observed (Fig. 5(c)). Deposition of Pb^{2+} on MNP@$Ni_xMn_{(0.5–x)}O$ was governed by the difference in its standard reduction potential from that of $PtCl_6^{2-}$ ions. The Pb^{2+} ions with a negative reduction potential (–0.13 V) were preferentially oxidized and deposited on MNP@$Ni_xMn_{(0.5–x)}O$. Deposition of metal ions as a function of their reduction potential was substantiated by selective reduction of $PtCl_6^{2-}$ ions on MNP@$Mn_xNi_{(0.5–x)}O$ (Fig. 5(d)). The $PtCl_6^{2-}$ ions with a positive reduction potential (0.73 V) were attracted to the electron–reinforced reduction centers on MNP@$Mn_xNi_{(0.5–x)}O$. Excellent charge carrier separation resulted in reduction of the $PtCl_6^{2-}$ ions to metallic Pt^0 in two steps as:

$$PtCl_6^{2-} + 2e^- \rightarrow PtCl_4^{2-} + 2Cl^- \quad (1)$$

$$2PtCl_4^{2-} \rightarrow PtCl_6^{2-} + Pt^0 + 2Cl^- \quad (2)$$

The Pt^{2+} peak in Fig. 5(d) was associated with the intermediate $PtCl_4^{2-}$ species, which was reduced to Pt^0 in step 2. Better insight into the selective and preferential interaction of metal ions with the nanocomposite was provided by irradiating a Pb^{2+}–$PtCl_6^{2-}$ solution containing equal masses of MNP@$Ni_xMn_{(0.5–x)}O$ and MNP@$Mn_xNi_{(0.5–x)}O$. The composite mixture was magnetically separated and analyzed using TEM. The two composites were distinguishable due to their distinct shell patterns in Fig. 5(e) and (f). EDS mapping showed the presence of Pb and Pt on MNP@$Ni_xMn_{(0.5–x)}O$ and MNP@$Mn_xNi_{(0.5–x)}O$, respectively. The selective deposition of metal ions on different composites agreed with the XPS results. Collectively, the XPS and EDS analysis verified the charge reversibility due to the inverted catalyst geometry. Complete oxidation and reduction of Pb and Pt, respectively, on different composites suggested excellent charge carrier separation. The ability of composites to preferentially/selectively maintain oxidation/reduction on the surface can have significant benefits for specific targeted photochemical applications.

Photoluminescence spectroscopy (PLS) was used to study charge carrier separation in the hierarchical catalyst. The nanocomposites were excited using a 300 nm laser, and the emission spectrum generated by relaxation of the excited electrons was recorded. An emission peak at 375 nm associated with excitonic recombination was observed in the spectra of all MNP@$Ni_xMn_{(0.5–x)}O$ composites (Fig. 6(a)). Pristine MNPs exhibited the highest photoluminescence intensity, which agreed with the typical high rate of recombination in Fe_3O_4. Charge carrier separation was improved after the growth of passivating silica shells and the first catalyst layer consisting of MnO (MNP@$Ni_0Mn_{0.5}O$). The first mixed precursor injection of Ni–Mn introduced additional energy levels, which delayed the electron relaxation in MNP@$Ni_{0.1}Mn_{0.4}O$. A decrease in photoluminescence was observed with increasing Ni–content in the composite. Oxygen vacancies associated with Ni–unit cells introduced traps for excited electrons that prolonged the electron lifetime in the composites. The most efficient charge separation was achieved in MNP@$Ni_{0.4}Mn_{0.1}O$. Increased photoluminescence in MNP@$Ni_{0.5}Mn_0O$ could be ascribed to: (i) the absence of Mn–related orbitals for electrons/holes and (ii) an increased mean path for transfer of holes from inner layers to the particle surface. A deep level emission (DLE) in the visible range (515–520 nm) appeared in the photoluminescence spectra (Fig. 6(b)). These emissions originated from indirect relaxation of the electrons excited via trap–states to the VBM. All Ni–containing composites showed DLE in their spectra, implying that the trap–states in the forbidden energy gap were generated by oxygen vacancies. The DLE peaks were red–shifted with increasing Ni–content in the composite, which could be due to an increase in the VBM in each successive layer. Photoluminescence results helped us understand the charge separation trends in composites and verified the role of oxygen vacancies in suppressing recombination.

The photocatalytic performance of the magnetic nanocomposite was evaluated in SMZ degradation. The composites were suspended in a 100 mg/L SMZ solution, and the change in SMZ concentration was monitored for 60 min. SMZ was persistent against UV irradiation that degraded 3–5% of the antibiotic contaminant in the control. Approximately 21% SMZ degradation was observed with the MNPs, coming at the expense of severe damage to the nanoparticle morphology as shown in Fig. S4(a) and (b). Growth of L1 (MNP@$Ni_0Mn_{0.5}O$) imparted minor and major improvement in the photocatalytic performance and

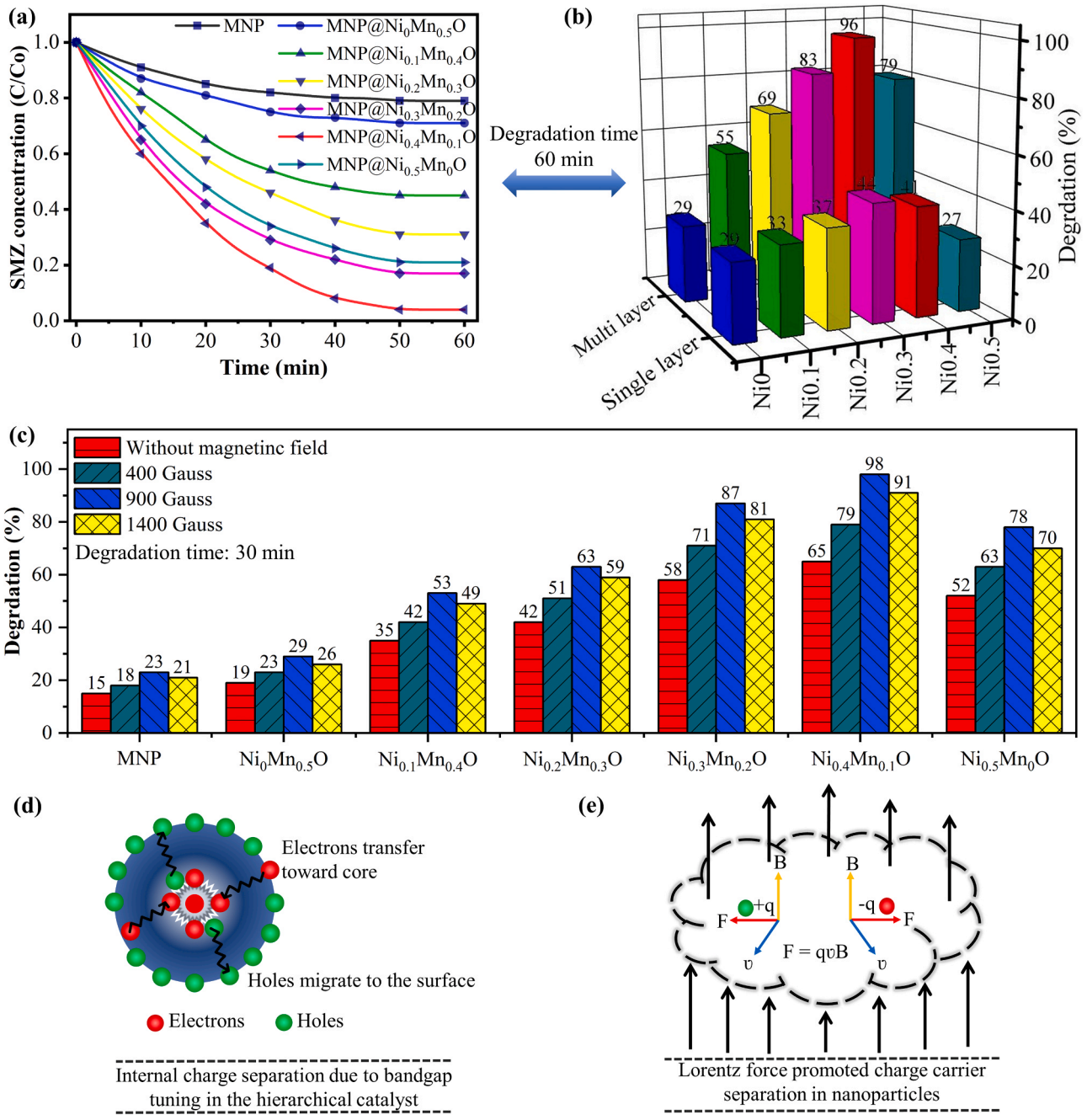

Fig. 7. (a) SMZ degradation by different composites in 60 min (without magnetic field). (b) Influence of multi-layer assembly on the catalytic properties (60 min, without magnetic field). (c) Effect of different magnetic field intensities on SMZ degradation in 30 min (d and e) Two main forces responsible for charge carrier separation in the hierarchical catalyst.

composite stability, respectively. Development of L2 laid the foundation for energy gradient–based charge separation. In Fig. 7(a), two–fold improvement in catalytic degradation of SMZ was observed with MNP@$Ni_{0.1}Mn_{0.4}O$ from L1. Charge carrier lifetime increased with the growth of successive catalyst layers. Enhanced charge separation associated with an internal electric field and oxygen vacancies led to 96% SMZ degradation with L5 (MNP@$Ni_{0.4}Mn_{0.1}O$). This excellent photocatalytic performance was achieved by optimization of Ni–Mn content, layer thickness, and surface oxygen vacancies in MNP@$Ni_{0.4}Mn_{0.1}O$. SMZ degradation dropped by 17% with L6 (MNP@$Ni_{0.5}Mn_0O$). This decrease was possibly due to the increased mean path for charge transfer and absence of heterojunctions on the surface of MNP@$Ni_{0.5}Mn_0O$. Photocatalytic performances by the composites followed a similar trend as the charge carrier lifetime predicted by the photoluminescence emission results. First order rate constants of SMZ degradation are listed in Table S1.

An interfacial electric field between the multiple catalyst layers regulates directional flow of charge carriers and inhibits recombination. The beneficial effect of the multiple layers was investigated using a single layer of the catalyst on the MNPs consisting of the same chemical composition as the outermost layer in the multi–layered catalysts. SMZ degradation results indicated a substantial improvement in catalytic activity due to charge separation in the multi–layered catalyst (Fig. 7 (b)). In single–layered catalysts, SMZ degradation reached the highest value of 44% with L4 (MNP@$Ni_{0.3}Mn_{0.2}O$). A slight improvement in degradation with increasing Ni–content was possible due to

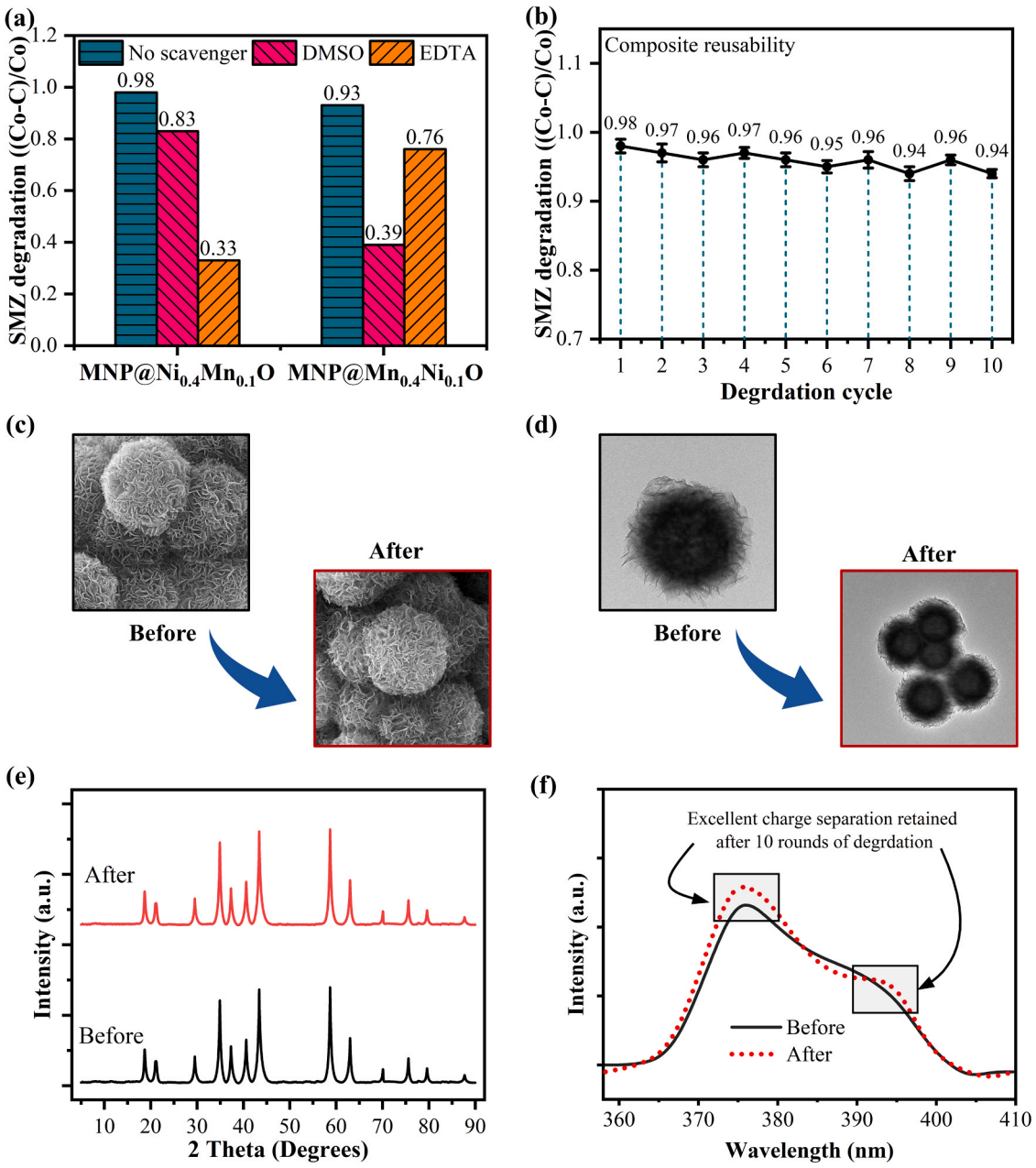

Fig. 8. (a) Scavenging experiment confirming the oxidative/reductive nature of surface–active sites. (b) Cyclic degradation tests showing the reusability potential of composites. (c) SEM images, (d) TEM images, (e) XRD spectra, and (f) PL spectra of MNP@$Ni_{0.4}Mn_{0.1}O$ before and after cyclic degradation experiments.

heterojunction formation, resulting in better charge separation. The multi–layered analog of MNP@$Ni_{0.4}Mn_{0.1}O$ exhibited a five–fold faster degradation rate (26.1×10^{-2} min^{-1}). Similarly, each multi–layer catalyst performed better than its single–layered equivalent. The difference in degradation results proved that the hypothesis for energy gradient–based charge separation was logical.

The effect of an external magnetic field on charge separation was studied in this research. Direct assessment of the magnetic field effect on recombination inhibition is difficult to identify/detect. Charge separation efficiency in response to a magnetic field–induced Lorentz force was evaluated with SMZ degradation in 30 min. Three levels were applied: a low magnetic field (400 Gauss, LMF), a medium magnetic field (900 Gauss, MMF), and a high magnetic field (1400 Gauss, HMF). Perturbation of the photocatalytic system at LMF exhibited improved SMZ degradation rate in Fig. 7(c). A roughly 20% higher SMZ degradation was observed for all composites at LMF. Since the magnetic field does not play any direct role in SMZ degradation, the Lorentz force–promoted charge separation was responsible for enhanced catalytic degradation. At MMF, MNP@$Ni_{0.4}Mn_{0.1}O$ recorded 98% SMZ degradation in 30 min, which translates to a substantial 50% increase in the catalytic activity from that without an external magnetic field. SMZ degradation results at LMF and MMF indicated a positive proportionality between the magnetic field and photocatalytic performance of the composites. At HMF, a $10 \pm 2\%$ drop in SMZ degradation from that at MMF was observed for all the composites. Theoretically, an increase in magnetic field strength should enhance the force being exerted on the charge carriers, which should supplement SMZ degradation. Performance deterioration at HMF suggested possible interference, countering the positive effect of an increase in magnetic field. A strong magnetic attraction disturbed the uniform composite suspension at HMF, and the composites formed clusters near the surface of the solution in Fig. S4(c). Nanoparticle agglomeration was not detected at LMF and MMF. The decrease in

catalytic activity due to agglomeration at HMF can limit the use of Lorentz force–based charge separation in ferromagnetic composites.

Complete charge separation in the hierarchical composite is summarized in Fig. 7(d and e). High rates of SMZ degradation were achieved with charge carrier separation as a function of (i) internal energy gradient and (ii) external magnetic field. The catalysts' intrinsic ability to separate charge carriers was developed by tuning the band edges in the multilevel catalyst by a series of precursor injections. In the $Ni_xMn_{(0.5-x)}O$ composite, band edges formed a gradient that supported transverse motion of charge carriers. Electrons with a natural tendency to drift down the energy slope were impelled to transfer toward the particle core. The surfaces of the nanoparticles were covered with holes, which were transferred up the energy ladder to yield a highly oxidative surface. The inherent charge separation efficiency was boosted by an external magnetic field. Charges moving with particles in the reaction mixture experienced a force that acted perpendicular to the plane formed between the direction of motion and the magnetic field (Fig. 7 (e)). According to the right–hand rule, this force propelled the oppositely charged excitons 180° apart. Inherent charge separation benefitted from the external force on excitons, which was reflected in SMZ degradation.

Charge reversibility as a function of inverted catalyst geometry was investigated in scavenging experiments. DMSO and EDTA were used to scavenge electrons and holes, respectively, in a typical experiment. Scavenging agents were added to the reaction mixture, and the change in SMZ concentration was monitored over time. As shown in Fig. 8(a), SMZ degradation by $MNP@Ni_{0.4}Mn_{0.1}O$ plummeted from 98% to 33% in the presence of EDTA, confirming the hole–dominant surface of the nanoparticles. The effect of DMSO on degradation was relatively smaller than that of EDTA. In a similar scavenging experiment, $MNP@Ni_{0.4}Mn_{0.1}O$ was replaced with its inverted counterpart ($MNP@Mn_{0.4}Ni_{0.1}O$). A reverse effect of scavenging agents occurred in SMZ degradation. DMSO caused a 54% decline in catalytic performance, indicating an electron rich surface. The reduced degradation by scavengers substantiated the catalysts' ability to: (i) generate reactive charge carriers, (ii) suppress recombination, and (iii) regulate selective oxidation/reduction at the particle surface depending upon the catalyst assembly and geometry. Excellent charge carrier generation and separation capacity were observed over extensive usage of the composite. The photocatalysts were magnetically separated after SMZ degradation, were washed and subjected to a subsequent degradation cycle. Approximately 94% degradation was monitored with $MNP@Ni_{0.4}Mn_{0.1}O$ in the tenth round, indicating a small loss of 4–6% in catalytic activity. This could be due to the negligible composite loss during recycling and minimal blocking of active sites by adsorbed contaminant/intermediates on the catalyst surface. The composite morphology and structural integrity were evaluated after 10 rounds of SMZ degradation. The hierarchical catalysts retained their original shape and contours. They were resistant to any significant damage due to stirring, irradiation, and magnetic separation in Fig. 8(c and d). XRD patterns showed that the crystalline features and phase of the composite did not change during prolonged exposure to photocatalytic conditions in Fig. 8(e). Likewise, the $MNP@Ni_{0.4}Mn_{0.1}O$ depicted similar PL trends, with minor changes in peak intensities, before and after the SMZ degradation cycles in Fig. 8(f). Overall, reusability experiments proved the composite's capacity to retain excellent catalytic activity and structural integrity, which could be critical in practical applications.

4. Conclusions

A hierarchical catalyst can be assembled on MNPs using a multiple precursor injection scheme. The composition of in–situ precursor injections govern the band edge tuning in the catalyst. Engineered band edges in the catalyst generate an energy gradient that regulates a directional drift of charge carriers towards the core/shell of nanoparticles. Highly active oxidation sites were generated by band gap engineering in $MNP@Ni_xMn_{(0.5-x)}O$. The oxidation sites in $MNP@Ni_xMn_{(0.5-x)}O$ can be converted to reduction sites by inverting the catalyst geometry to form $MNP@Mn_xNi_{(0.5-x)}O$. The multi–layered catalyst outperforms its single–layered counterpart due to prolonged charge carrier lifetimes. A magnetic field enhances the inherent catalytic potential by exerting a force in opposite directions for electrons and holes. Optimization of the magnetic field intensity is crucial to realize the complete benefits of the Lorentz force supported charge separation. Overall, the fabrication scheme, charge reversibility, magnetic separation, and Lorentz force assisted charge separation in $MNP@Ni_xMn_{(0.5-x)}O$ make it very practical for photochemical applications.

CRediT authorship contribution statement

Hassan Anwer: Conceptualization; Writing – Original Draft. **Jae-Woo Park:** Writing – Review & Editing; Funding acquisition.

Declaration of Competing Interest

The authors declare that they have no known competing financial interests or personal relationships that could have appeared to influence the work reported in this paper.

Acknowledgments

This study was supported by the Basic Science Research Program through the National Research Foundation of Korea (NRF) funded by the Ministry of Science, ICT, & Future Planning (No. 2018R1A2A1A05023555) and the Korea Environmental Industry and Technology Institute (KEITI) through The Technology Development Project to secure the health of aquatic ecosystems, funded by Korea Ministry of Environment (No.2021003040004).

Appendix A. Supporting information

Supplementary data associated with this article can be found in the online version at doi:10.1016/j.apcatb.2021.120724.

References

[1] S. Yue, L. Li, S.C. McGuire, N. Hurley, S.S. Wong, Metal chalcogenide quantum dot-sensitized 1D-based semiconducting heterostructures for optical-related applications, Energy Environ. Sci. 12 (2019) 1454–1494.
[2] X. Zheng, L. Zhang, Photonic nanostructures for solar energy conversion, Energy Environ. Sci. 9 (2016) 2511–2532.
[3] Y. Wen Teh, Y. Wei Goh, X. Ying Kong, B.-J. Ng, S.-T. Yong, S.-P. Chai, Fabrication of Bi2WO6/Cu/WO3 all-solid-state Z-scheme composite photocatalyst to improve CO_2 photoreduction under visible light irradiation, ChemCatChem 11 (2019) 6431–6438.
[4] C. Wang, X. Liu, W. He, Y. Zhao, Y. Wei, J. Xiong, J. Liu, J. Li, W. Song, X. Zhang, Z. Zhao, All-solid-state Z-scheme photocatalysts of g-C3N4/Pt/macroporous-(TiO2@carbon) for selective boosting visible-light-driven conversion of CO_2 to CH4, J. Catal. 389 (2020) 440–449.
[5] Z. Xie, Y. Feng, F. Wang, D. Chen, Q. Zhang, Y. Zeng, W. Lv, G. Liu, Construction of carbon dots modified MoO3/g-C3N4 Z-scheme photocatalyst with enhanced visible-light photocatalytic activity for the degradation of tetracycline, Appl. Catal. B Environ. 229 (2018) 96–104.
[6] W. Zhao, J. Li, B. Dai, Z. Cheng, J. Xu, K. Ma, L. Zhang, N. Sheng, G. Mao, H. Wu, K. Wei, D.Y.C. Leung, Simultaneous removal of tetracycline and Cr(VI) by a novel three-dimensional AgI/BiVO4 p-n junction photocatalyst and insight into the photocatalytic mechanism, Chem. Eng. J. 369 (2019) 716–725.
[7] M. Mehdi Sabzehmeidani, H. Karimi, M. Ghaedi, CeO2 nanofibers-CdS nanostructures n–n junction with enhanced visible-light photocatalytic activity, Arab. J. Chem. 13 (2020) 7583–7597.
[8] S. Kumar, V. Pandit, K. Bhattacharyya, V. Krishnan, Sunlight driven photocatalytic reduction of 4-nitrophenol on Pt decorated ZnO-RGO nanoheterostructures, Mater. Chem. Phys. 214 (2018) 364–376.
[9] X. Zhou, Q. Gao, S. Yang, Y. Fang, Carbon nanotube@silicon carbide coaxial heterojunction nanotubes as metal-free photocatalysts for enhanced hydrogen evolution, Chin. J. Catal. 41 (2020) 62–71.

[10] Y. Luo, X. Yan, J. Zhang, B. Li, Y. Wu, Q. Lu, C. Jin, X. Zhang, X. Ren, A graphene/single GaAs nanowire Schottky junction photovoltaic device, Nanoscale 10 (2018) 9212–9217.
[11] M.D. Purkayastha, S. Sil, N. Singh, P.P. Ray, G.K. Darbha, S. Bhattacharyya, A. I. Mallick, T.P. Majumder, Sonochemical synthesis of nanospherical TiO2 within graphene oxide nanosheets and its application as a photocatalyst and a Schottky diode, FlatChem 22 (2020), 100180.
[12] Y. Yang, Z. Zeng, G. Zeng, D. Huang, R. Xiao, C. Zhang, C. Zhou, W. Xiong, W. Wang, M. Cheng, W. Xue, H. Guo, X. Tang, D. He, Ti3C2 Mxene/porous g-C3N4 interfacial Schottky junction for boosting spatial charge separation in photocatalytic H2O2 production, Appl. Catal. B Environ. 258 (2019), 117956.
[13] J. Li, P. Jiménez-Calvo, E. Paineau, M.N. Ghazzal, Metal chalcogenides based heterojunctions and novel nanostructures for photocatalytic hydrogen evolution, Catalysts 10 (2020) 89.
[14] L. Xiao, Q. Zhang, P. Chen, L. Chen, F. Ding, J. Tang, Y.-J. Li, C.-T. Au, S.-F. Yin, Copper-mediated metal-organic framework as efficient photocatalyst for the partial oxidation of aromatic alcohols under visible-light irradiation: synergism of plasmonic effect and schottky junction, Appl. Catal. B Environ. 248 (2019) 380–387.
[15] J. Li, Xa Dong, Y. Sun, W. Cen, F. Dong, Facet-dependent interfacial charge separation and transfer in plasmonic photocatalysts, Appl. Catal. B Environ. 226 (2018) 269–277.
[16] H. Sayılkan, Improved photocatalytic activity of Sn4+-doped and undoped TiO2 thin film coated stainless steel under UV- and VIS-irradiation, Appl. Catal. A Gen. 319 (2007) 230–236.
[17] X. Kong, M. Qiu, A. Wang, L. Yang, R. Zhou, Y. Fan, D. Kong, C. Gu, Influence of alumina binders on adhesion and cohesion during preparation of Cu-SAPO-34/monolith catalysts, Int. J. Appl. Ceram. Technol. 15 (2018) 1490–1501.
[18] Y. Wang, Z. Huang, R.S. Gurney, D. Liu, Superhydrophobic and photocatalytic PDMS/TiO2 coatings with environmental stability and multifunctionality, Colloids Surf. A Physicochem. Eng. Asp. 561 (2019) 101–108.
[19] S. Ramasundaram, M.G. Seid, H.-E. Kim, A. Son, C. Lee, E.-J. Kim, S.W. Hong, Binder-free immobilization of TiO2 photocatalyst on steel mesh via electrospraying and hot-pressing and its application for organic micropollutant removal and disinfection, J. Hazard. Mater. 360 (2018) 62–70.
[20] L. Zhang, Y. Zhang, S. Huang, Y. Yuan, H. Li, Z. Jin, J. Wu, Q. Liao, L. Hu, J. Lu, S. Ruan, Y.-J. Zeng, Co3O4/Ni-based MOFs on carbon cloth for flexible alkaline battery-supercapacitor hybrid devices and near-infrared photocatalytic hydrogen evolution, Electrochim. Acta 281 (2018) 189–197.
[21] S. Obregón, G. Amor, A. Vázquez, Electrophoretic deposition of photocatalytic materials, Adv. Colloid Interface Sci. 269 (2019) 236–255.
[22] S. Vignesh, S. Suganthi, J. Kalyana Sundar, V. Raj, Construction of α-Fe2O3/CeO2 decorated g-C3N4 nanosheets for magnetically separable efficient photocatalytic performance under visible light exposure and bacterial disinfection, Appl. Surf. Sci. 488 (2019) 763–777.
[23] J. Ni, J. Xue, L. Xie, J. Shen, G. He, H. Chen, Construction of magnetically separable NiAl LDH/Fe3O4–RGO nanocomposites with enhanced photocatalytic performance under visible light, Phys. Chem. Chem. Phys. 20 (2018) 414–421.
[24] Z. Shao, T. Zeng, Y. He, D. Zhang, X. Pu, A novel magnetically separable CoFe2O4/Cd0.9Zn0.1S photocatalyst with remarkably enhanced H2 evolution activity under visible light irradiation, Chem. Eng. J. 359 (2019) 485–495.
[25] N. Chandel, K. Sharma, A. Sudhaik, P. Raizada, A. Hosseini-Bandegharaei, V. K. Thakur, P. Singh, Magnetically separable ZnO/ZnFe2O4 and ZnO/CoFe2O4 photocatalysts supported onto nitrogen doped graphene for photocatalytic degradation of toxic dyes, Arab. J. Chem. 13 (2020) 4324–4340.
[26] E. Abroshan, S. Farhadi, A. Zabardasti, Novel magnetically separable Ag3PO4/MnFe2O4 nanocomposite and its high photocatalytic degradation performance for organic dyes under solar-light irradiation, Sol. Energy Mater. Sol. Cells 178 (2018) 154–163.
[27] R. Liu, Y. Zhao, R. Huang, Y. Zhao, H. Zhou, Multiferroic ferrite/perovskite oxide core/shell nanostructures, J. Mater. Chem. 20 (2010) 10665–10670.
[28] Y. Wang, S. Li, X. Xing, F. Huang, Y. Shen, A. Xie, X. Wang, J. Zhang, Self-assembled 3D flowerlike hierarchical Fe3O4@Bi2O3 core–shell architectures and their enhanced photocatalytic activity under visible light, Chem. – Eur. J. 17 (2011) 4802–4808.
[29] X.-M. He, C.-W. Zhang, F.-F. Guo, S.-M. Yan, Y.-T. Li, L.-Q. Liu, H.-G. Zhang, Y.-W. Du, W. Zhong, Exchange-biased hybrid γ-Fe2O3/NiO core–shell nanostructures: three-step synthesis, microstructure, and magnetic properties, Phys. Chem. Chem. Phys. 21 (2019) 11967–11976.
[30] G. Xi, B. Yue, J. Cao, J. Ye, Fe3O4/WO3 hierarchical core–shell structure: high-performance and recyclable visible-light photocatalysis, Chem. – Eur. J. 17 (2011) 5145–5154.
[31] X. Li, S. Song, X. Wang, D. Liu, H. Zhang, Self-assembled 3D flower-like hierarchical Fe3O4/KxMnO2 core–shell architectures and their application for removal of dye pollutants, CrystEngComm 14 (2012) 2866–2870.
[32] N.S. Gultom, H. Abdullah, D.-H. Kuo, Effects of graphene oxide and sacrificial reagent for highly efficient hydrogen production with the costless Zn(O,S) photocatalyst, Int. J. Hydrog. Energy 44 (2019) 29516–29528.
[33] A.J. Jafari, H. Arfaeinia, B. Ramavandi, R.R. Kalantary, A. Esrafily, Ozone-assisted photocatalytic degradation of gaseous toluene from waste air stream using silica-functionalized graphene oxide/ZnO coated on fiberglass: performance, intermediates, and mechanistic pathways, Air Quality, Atmosphere Health 12 (2019) 1181–1188.
[34] F. Hayati, A.A. Isari, B. Anvaripour, M. Fattahi, B. Kakavandi, Ultrasound-assisted photocatalytic degradation of sulfadiazine using MgO@CNT heterojunction composite: effective factors, pathway and biodegradability studies, Chem. Eng. J. 381 (2020), 122636.
[35] E. Zarei, R. Ojani, Fundamentals and some applications of photoelectrocatalysis and effective factors on its efficiency: a review, J. Solid State Electrochem. 21 (2017) 305–336.
[36] X. Zhao, W. Gao, Q. Liu, C. Cui, W. Zhou, X. Wang, X.L. Zhang, L. Zhao, Y. Sang, H. Liu, Enhanced photo-induced carrier separation of CdS/MoS2 via micro-potential of Mo microsheet derived from electromagnetic induction, Chem. Eng. J. 404 (2021), 126972.
[37] J. Li, Q. Pei, R. Wang, Y. Zhou, Z. Zhang, Q. Cao, D. Wang, W. Mi, Y. Du, Enhanced photocatalytic performance through magnetic field boosting carrier transport, ACS Nano 12 (2018) 3351–3359.
[38] F. Lu, J. Wang, J. Li, Y. Du, X.-P. Kong, S. Liu, D. Yi, Y.K. Takahashi, K. Hono, X. Wang, J. Yao, Regulation of oxygen reduction reaction by the magnetic effect of L10-PtFe alloy, Appl. Catal. B Environ. 278 (2020), 119332.
[39] T. Luo, J. Wan, Y. Ma, Y. Wang, Y. Wan, Sulfamethoxazole degradation by an Fe (ii)-activated persulfate process: insight into the reactive sites, product identification and degradation pathways, Environ. Sci. Process. Impacts 21 (2019) 1560–1569.
[40] L. Jia, Y. Kitamoto, Influence of silica coating process on fine structure and magnetic properties of iron oxide nanoparticles, Electrochim. Acta 183 (2015) 148–152.
[41] K. Jazbec, M. Šala, M. Mozetič, A. Vesel, M. Gorjanc, Functionalization of cellulose fibres with oxygen plasma and ZnO nanoparticles for achieving UV protective properties, J. Nanomater. 2015 (2015) 1–9.
[42] M.D.S. Pires, F.G.E. Nogueira, J.A. Torres, L.C.T. Lacerda, S. Corrêa, M.C. Pereira, T.C. Ramalho, Experimental and theoretical study on the reactivity of maghemite doped with Cu2+ in oxidation reactions: structural and thermodynamic properties towards a Fenton catalyst, RSC Adv. 6 (2016) 80830–80839.
[43] X. Tang, J. Huang, K. Liu, Q. Feng, Z. Li, M. Ao, Synthesis of magnetically separable MnO2/Fe3O4/silica nanofiber composite with enhanced Fenton-like catalytic activity for degradation of Acid Red 73, Surf. Coat. Technol. 354 (2018) 18–27.
[44] S.S. Kalanur, I.-H. Yoo, I.-S. Cho, H. Seo, Effect of oxygen vacancies on the band edge properties of WO3 producing enhanced photocurrents, Electrochim. Acta 296 (2019) 517–527.
[45] M.T. Greiner, Z.-H. Lu, Thin-film metal oxides in organic semiconductor devices: their electronic structures, work functions and interfaces, NPG Asia Mater. 5 (2013), e55.